Electronic Supplementary Material (ESI) for Materials Chemistry Frontiers.

Electronic Supporting Information

Regulating the adsorption behavior of intermediates on Ir-W@Ir-WO_{3-x} boosts acidic water oxidation electrocatalysis

Zheng Lu, [#] Cong Wei, [#] Xinmiao Liu, Yanyan Fang, Xiaobin Hao, Yipeng Zang, Zhibin Pei, Jinyan Cai, Yishang Wu, Di Niu, Amirabbas Mosallanezhad, Da Sun, Jian Ye, Shuwen Niu,* and Gongming Wang*

Hefei National Laboratory for Physical Science at the Microscale, Department of Chemistry, University of Science and Technology of China, Hefei, Anhui, 230026, P. R. China.

[#]These authors contributed equally to this work.

Corresponding author. E-mail: wanggm@ustc.edu.cn, niusw@mail.ustc.edu.cn.

Experimental Section

Synthesis of materials

Synthesis of Ir-WO_3 NWs. The Ir-WO_3 NWs was prepared via a modified hydrothermal reaction.[1] Typically, 35 mmol oxalic acid dihydrate ($H_2C_2O_4 \cdot 2H_2O$) was added into 100 mL 12.5 mM sodium tungstate (VI) dihydrate ($Na_2WO_4 \cdot 2H_2O$) aqueous solution and the pH was adjusted to 1.2 by the addition of 1 M H_2SO_4 solution. The mixed solution was then diluted to 250 mL to obtain H_2WO_4 solution. Subsequently, 12 mmol ammonium sulfate ($(NH_4)_2SO_4$) and 0.1 mmol hydrogen hexachloroiridate (IV) hexahydrate ($H_2IrCl_6 \cdot 6H_2O$) were added into 20 mL of H_2WO_4 solution. Then the as-prepared solution and a piece of carbon cloth were transferred into a 25 mL autoclave vessel and maintained at 180 °C for 18 h. Finally, the prepared Ir-WO_3 NWs on carbon cloth were obtained after washing carefully with deionized (DI) water and drying at 60 °C for 12 h in a vacuum oven. To increase the degree of crystallinity, the prepared Ir-WO_3 NWs were finally annealed at 600 °C for 30 min in air atmosphere.

Synthesis of WO_3 NWs. The WO_3 NWs was fabricated using the same procedure with Ir-WO_3 except the addition of $H_2IrCl_6 \cdot 6H_2O$.

Synthesis of Ir-W@Ir-WO_{3-x} NPs. The Ir-W@Ir-WO_{3-x} NPs were prepared by reducing the Ir-WO_3 NWs at 700 °C for 36 h in a home-built tube furnace system under the atmosphere of 3% H_2/Ar.

Materials Characterization

The X-ray powder diffraction (XRD, Philips, X'pert X-ray) of the samples were collected on a diffractometer using Cu Kα radiation ($\lambda = 1.54178$ Å). Scanning electron microscopy (SEM) was carried out on a JSM-6700F electron microscope. The transmission electron microscope (TEM) images were obtained with Hitachi H7650. Inductively coupled plasma atomic emission spectroscopy (ICP-AES) was performed on a Perkin-Elmer Optima 7300 DV ICP spectrometer. The high-resolution transmission electron microscopy (HRTEM), high-angle annular dark-field scanning transmission electron microscopy (HAADF-STEM) and the energy dispersive X-ray spectroscopy (EDX) analysis were conducted on JEM-ARM-2100 F. Raman spectra were recorded on a Lab-RAM HR system with 633 nm excitation. X-ray photoelectron spectroscopy (XPS) data was collected at the photoemission end-station (BL10B) in the National Synchrotron Radiation Laboratory (NSRL), Hefei. The surface area plots were collected by Brunauer-Emmett-Teller (BET, Micromeritics ASAP 2020).

Electrochemical measurements

All the electrochemical measurements were performed in a three-electrode system on the CHI760E with 0.5 M H_2SO_4 solution as electrolyte. The studied material grown on carbon cloth worked as working electrode, while Ag/AgCl (saturated KCl solution) electrode and platinum plate were employed as reference and counter electrodes, respectively. The loading amounts of Ir-W@Ir-WO_{3-x} NPs is 3.7 mg cm^{-2}. For comparision, commercial IrO_2 was also prepared as working electrode and the details were provided below. The IrO_2 catalyst ink with a concentration of 4 mg mL^{-1} was prepared by ultrasonically dispersing 4 mg IrO_2 and 10 µL Nafion solution (5 wt%) in 1 mL water (850 µL)/ethanol (150 µL) solution. Then, the catalyst ink was coated onto the carbon cloth with a IrO_2 loading amount of 4 mg cm^{-2}. All the potential versus Ag/AgCl were converted with respect to the reversible hydrogen electrode (RHE) according to the Nernst equation: E (vs. RHE) = E (vs. Ag/AgCl) + E^0 (Ag/AgCl) + 0.059 * pH. The LSV curves were performed with the scan rate of 5 mV s^{-1} and were further calibrated with iR correction ($E_{iR\text{-}corrected} = E_{original} - i^*R$). The electrochemical impedance spectroscopy (EIS) measurements were conducted at the potential of 1.31 V vs. RHE in the frequency range from 100 kHz to 0.01 Hz. The chronopotentiometric (CP) test for stability studies was carried out at the constant current density of 10 mA cm^{-2}. The electrochemical surface areas of the catalysts were collected by conducting cyclic voltammetry (CV) in the potential range of 0.9-1.02 V vs. RHE with various scan rates from 10 to 80 mV s^{-1}. The current differences were plotted against scan rates, in which the C_{dl} could be obtained from the slope.

The TOF values were calculated by a previously reported method.[2]

$$\mathrm{TOF}=\frac{\text{number of total oxygen turnover /cm}^2\text{ of geometric area}}{\text{number of active sites /cm}^2\text{ of geometric area}}$$

The number of total oxygen turnover (No. of O_2) was calculated by the following equation:

$$\text{No. of } O_2 = \left(j\frac{\text{mA}}{\text{cm}^2}\right)*\left(\frac{1\text{ C s}^{-1}}{1000\text{ mA}}\right)*\left(\frac{1\text{ mol e}^-}{96485.3\text{ C}}\right)*\left(\frac{1\text{mol O}_2}{4\text{ mol e}^-}\right)*\left(\frac{6.022 * 1023\text{ O}_2\text{ molecules}}{1\text{ mol O}_2}\right)$$

$$=1.56*10^{15}\text{ s}^{-1}\text{ cm}^{-2}\text{ per}\frac{\text{mA}}{\text{cm}^2}$$

The numbers of active sites were estimated as the number of surface sites (including Ir, W, and O as possible active sites). The active sites per real surface area was calculated from the following equation:

$$\text{Number of active sites} = \left(\frac{\text{number of atoms per unit cell}}{\text{volume per unit cell}}\right)^{\frac{2}{3}}$$

$$\text{Number of active sites (Ir-W@Ir-WO}_{3-x}\text{)} = \left(\frac{47}{654.1\text{ Å}^3}\right)^{\frac{2}{3}} = 0.1728\text{ Å}^{-2}$$

$$= 1.728*10^{15}\text{ atoms cm}^{-2}$$

$$\text{Number of active sites (Ir-WO}_3\text{)} = \left(\frac{143}{1872\text{ Å}^3}\right)^{\frac{2}{3}} = 0.1800\text{ Å}^{-2} = 1.8*10^{15}\text{ atoms cm}^{-2}$$

$$\text{Number of active sites (IrO}_2\text{)} = \left(\frac{6}{65.26\text{ Å}^3}\right)^{\frac{2}{3}} = 0.2027\text{ Å}^{-2} = 2.027*10^{15}\text{ atoms cm}^{-2}$$

Then, the TOF plot can be obtained from LSV curves by the following formula:

TOF= $\frac{\left(1.56 * 10^{15}\ \mathrm{s^{-1}cm^{-2}}\ \mathrm{per}\ \frac{\mathrm{mA}}{\mathrm{cm^{2}}}\right) * |j|}{\text{number of active sites} * A_{ECSA}}$, where the A_{ECSA} is the electrochemical surface area, which can be estimated based on the electro-chemical double layer capacitance following the equation:

A_{ECSA} = $\frac{\text{specific capacitance}}{40\ \mu\mathrm{F\ cm^{-2}}}$, where specific capacitance is C_{dl} and 40 μF cm^{-2} is a constant to calculate the ECSA.

Method of hydroperoxide detection

Standard curve collection. Firstly, 250 μL 0.07 M $CoSO_4$ solution and 9.5 mL 2 M $KHCO_3$ solution were mixed and stirred for 10 min to prepare color developing agent (CPA).[3] Then commercial hydroperoxide solution was diluted to various concentrations of 0.602, 1.204, 3.01 and 6.02 μg mL^{-1} with DI water. Subsequently, 500 μL diluted hydroperoxide solutions were mixed with the prepared CPA solution, respectively. The mixed solutions were kept for 30 min and followed by the ultraviolet-visible (UV-vis) spectroscopy test, respectively. Finally, the UV-vis data were collected and calculated to obtain the standard curve (Fig. S14).

Concentration estimation of hydroperoxide. The CPA solutions were prepared using the same procedure. The electrolyte solutions with the volume of 60 mL were collected after 30 min CP test at the current density of 10 mA cm^{-2} using Ir-WO_3 NWs, Ir-W@Ir-WO_{3-x} NPs and WO_3 NWs as the working electrode, respectively. Pipetting 500 μL electrolyte solution and mixing with the CPA solution. The above mixed solutions were kept for 30 min and followed by the UV-vis spectroscopy test. The concentrations of hydroperoxide in various electrolytes were calculated according to the calibration equation obtained from the standard calibration curve in Fig. S14.

Method for calculation of the leached metal ions percent from electrodes

The leached percent of iridium and tungsten were calculated through the following equation[4]:

$$\text{Leached ion percent} = \frac{c_{post}}{c_{pre}} * 100\%;$$

Where the c_{post} represented the concentration of iridium and tungsten in electrolyte after CP test for different time, while the c_{pre} was the concentration of iridium and tungsten on the fresh electrodes, both of which were collected via ICP-AES.

Density functional theory (DFT) calculations

The DFT calculations with the projector-augmented wave (PAW) method[5, 6] were carried out using the Vienna ab initio Simulation Package (VASP) in this study. The Perdew-Burke-Ernzerhof (PBE) functional of generalized gradient approximation (GGA) of was adopted for the exchange-correlation energy and the DFT-D3 approach for the long-range van der Waals interaction.[7, 8] The kinetic energy cutoff for a plane wave basis was set as 450 eV. The surface Brillouin zone was sampled by a 3 × 3 × 1 k-points grid for the structure optimizations. The electron smearing was employed via the Methfessel-Paxton technique with a smearing width of 0.05 eV. The geometry optimization would be converged when the energy differences were smaller than 5.0×10^{-6} eV, and the forces were less than 0.03 eV/Å.

The overpotential was evaluated using a previously described approach OER occur via the following steps:

$$2H_2O + * \rightarrow OH^* + H_2O + H^+ + e^- \tag{1}$$

$$OH^* + H_2O \rightarrow O^* + H_2O + H^+ + e^- \tag{2}$$

$$O^* + H_2O \rightarrow OOH^* + H^+ + e^- \tag{3}$$

$$OOH^* \rightarrow O_2 + H^+ + e^- \tag{4}$$

where * represents the preferable adsorption site for intermediates.

In our calculations, the corrected energy for adsorbents and free gas at standard conditions (U = 0, pH = 0, p = 1 bar, T = 298.15 K), the free energy was obtained by VASPKIT tool. Therefore, the reaction free energy of each step is calculated by

$$\Delta G = \Delta E + \Delta ZPE - T\Delta S \tag{5}$$

where ΔE, ΔZPE and ΔS refer the total energy obtained from DFT calculation zero-point energy correction, and the vibrational entropy change, respectively. For the adsorbed species, the translational and rotational modes are treated as the special cases of vibrational modes.[5] Therefore，the zero-point vibrational energy (*ZPE*) and vibrational entropy (*S*) are obtained according to the equations (6) and (7):

$$\Delta ZPE = \sum_{i}^{\text{Vibrations}} \left[\frac{hv_i}{2} \right] \tag{6}$$

$$S = S_{vib} = R \sum_{i=1}^{\text{vibration}} \left[- \ln(1 - e^{-hv_i/k_BT}) + \frac{hv_i/k_B}{e^{-hv_i/k_BT} - 1} \right] \tag{7}$$

The overpotential (η) can be evaluated from the Gibbs free energy differences of each step as:

$$\eta = \max [\Delta G_1, \Delta G_2, \Delta G_3, \Delta G_4]/e - 1.23 \text{ V} \tag{8}$$

where ΔG_1, ΔG_2, ΔG_3 and ΔG_4 are the free energy of reactions (1) to (4).

Surface models. Based on the experimental characterization results, a series of heterojunctions were constructed to simulate the core-shell Ir-W@Ir-WO_{3-x} catalyst consisting of Ir-WO_{3-x} shell and Ir-W metallic core. The crystalline structure of the Ir-W@Ir-WO_{3-x} NPs is W cubic phase, in which the (110) surface is the main surface. Therefore, the cubic W (110) with specific replacement of Ir as the metallic core model and a layer of Ir-WO_{3-x} on the surface to simulate the amorphous oxide shell. Among them, Ir-WO_{3-x} shells were simulated by substituting a W atom with Ir atom in WO_3 (001) surfaces with or without oxygen vacancy, Ir-W metallic cores were simulated by three surface models, including WO_3 (110) surface with or without Ir doping, in which the Ir-doped WO_3 (110) surfaces include surface layer doped Ir atom and the subsurface layer doped Ir atom. To sum up, five different surface models are considered for the combining Ir-WO_{3-x} shell and Ir-W metallic core, which are denoted W@Ir-WO_3 (110), W@Ir-WO_3-O_v (110), Ir_{sur}-W@Ir-WO_3 (110), Ir_{sur}-W@Ir-WO_3-O_v (110) and Ir_{sub}-W@Ir-WO_3-O_v (110) (Fig. S15), respectively. In addition, WO_3 (001) and Ir-WO_3 (001) were considered as control groups to simulate WO_3 and Ir-WO_3 catalysts because WO_3 (001) is the most stable facet and widely adopted for DFT study of adsorption behavior.[9,10]

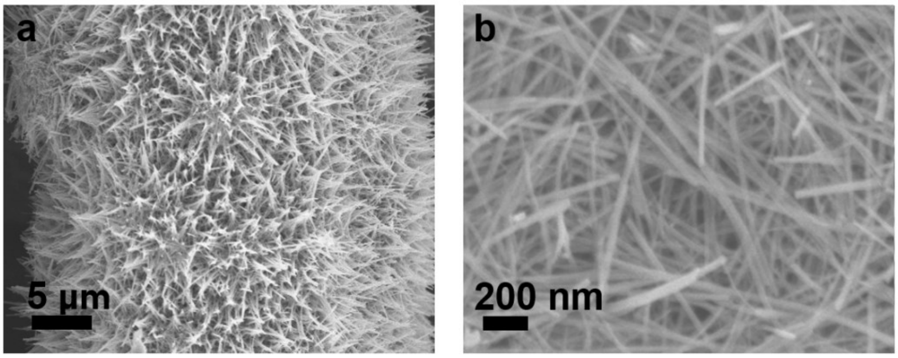

Fig. S1. (a, b) SEM images of Ir-WO_3 NWs.

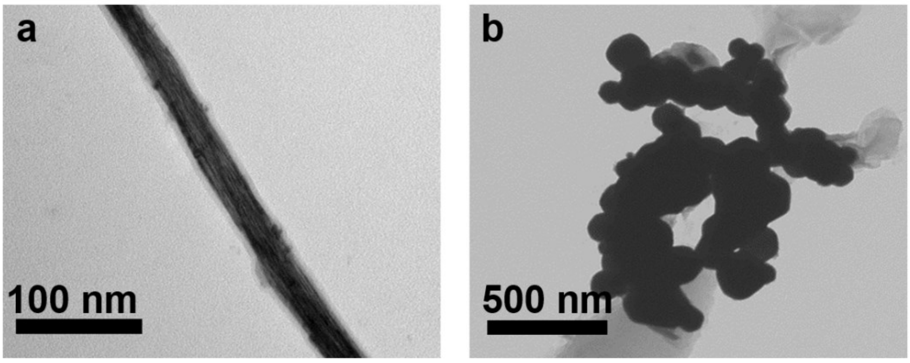

Fig. S2. (a) TEM image of Ir-WO_3 NWs. (b) TEM image of Ir-W@Ir-WO_{3-x} NPs.

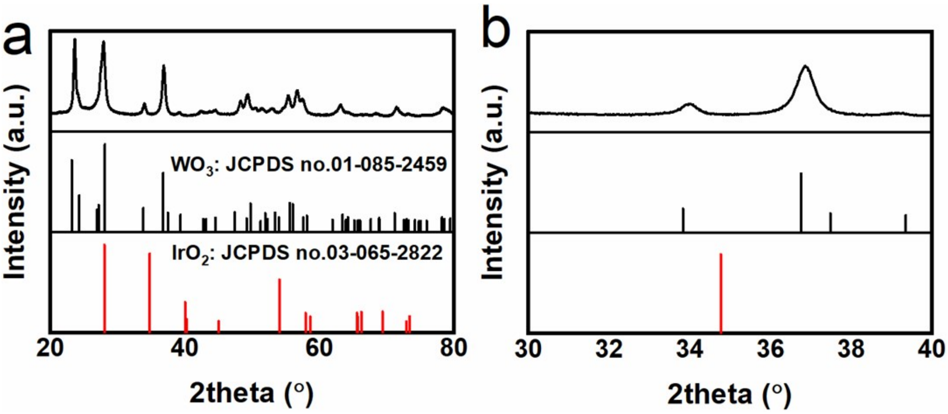

Fig. S3. (a, b) XRD patterns of Ir-WO_3 NWs and the corresponding magnification of the diffraction peaks.

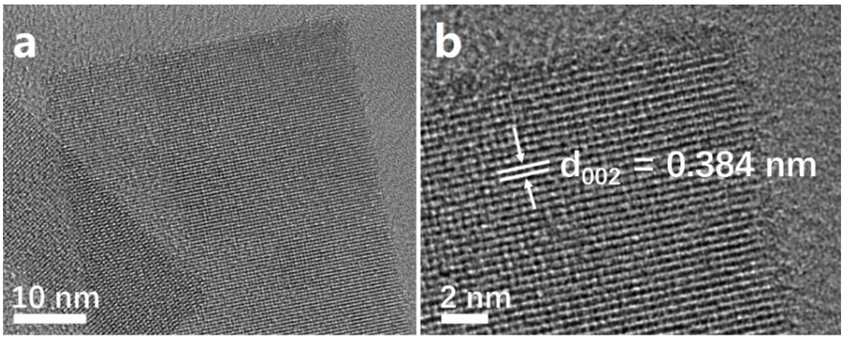

Fig. S4. HRTEM images of Ir-WO_3 NWs.

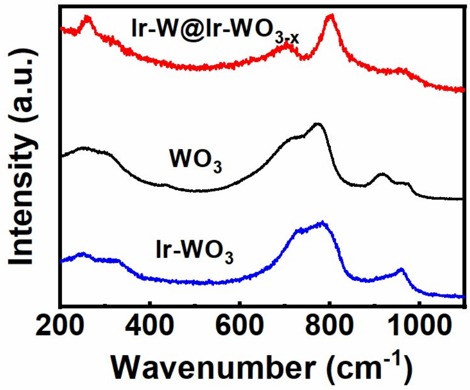

Fig. S5. Raman spectra of Ir-W@Ir-WO_{3-x}, Ir-WO_3 and WO_3.

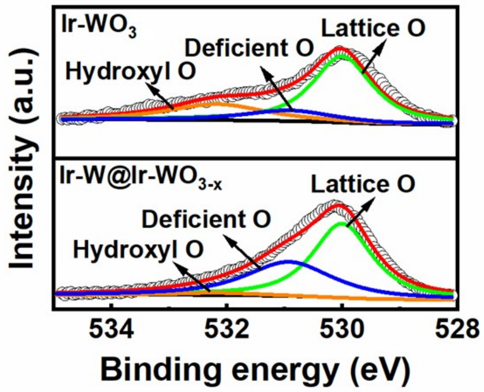

Fig. S6. XPS O 1s spectra and the corresponding fitting curves of Ir-WO_3 and Ir-W@Ir-WO_{3-x}.

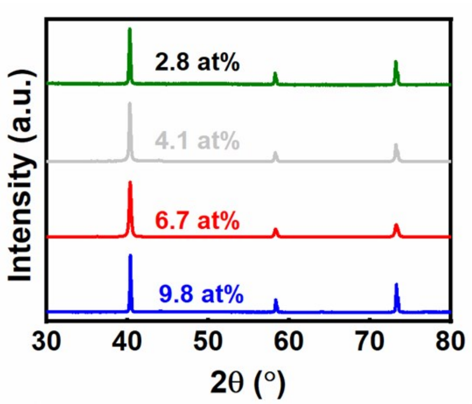

Fig. S7. XRD patterns of Ir-W@Ir-WO$_{3-x}$ with different Ir ratios.

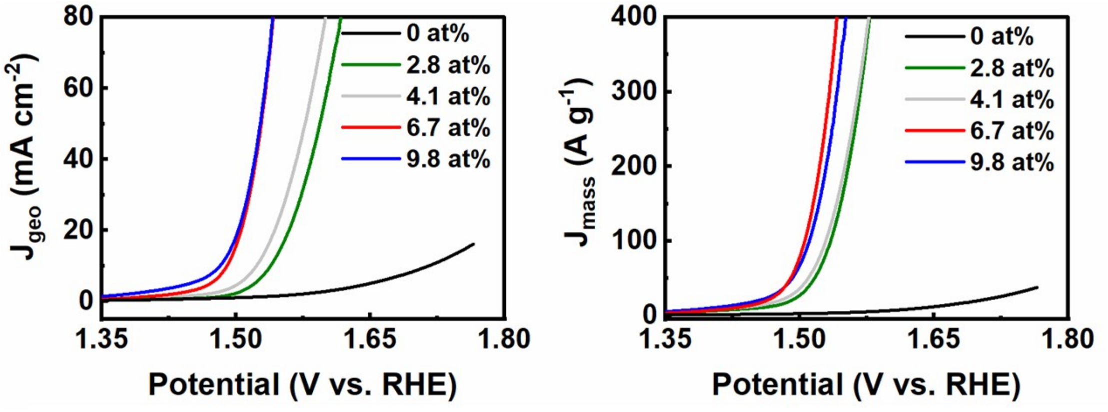

Fig. S8. LSV curves of Ir-W@Ir-WO$_{3-x}$ with different Ir ratios.

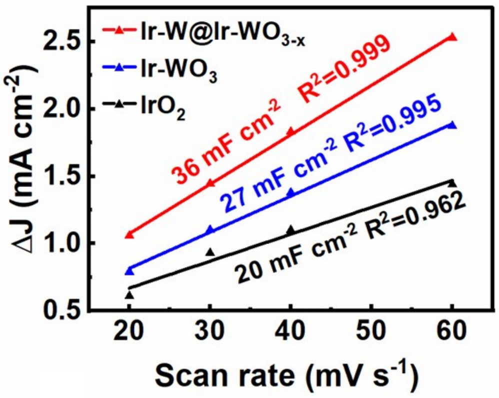

Fig. S9. The capacitive currents as a function of scan rate of Ir-W@Ir-WO$_{3-x}$, Ir-WO$_3$ and IrO$_2$.

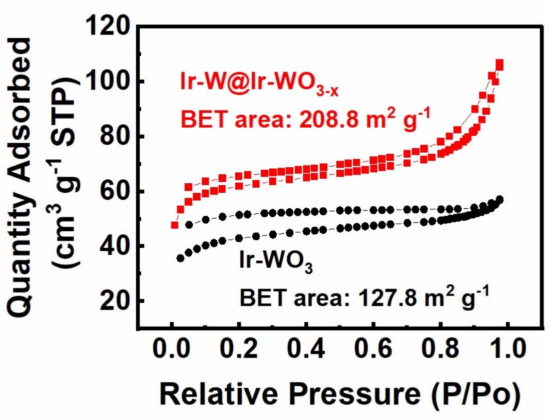

Fig. S10. Nitrogen adsorption and desorption isotherms plots of Ir-WO$_3$ and Ir-W@Ir-WO$_{3-x}$.

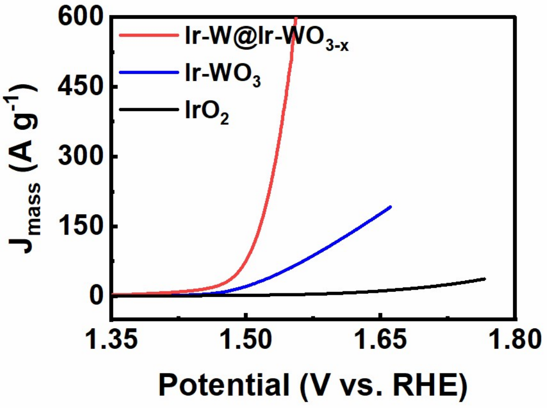

Fig. S11. LSV curves of Ir-W@Ir-WO$_{3-x}$, Ir-WO$_3$ and IrO$_2$ normalized by the mass of the iridium on the working electrodes.

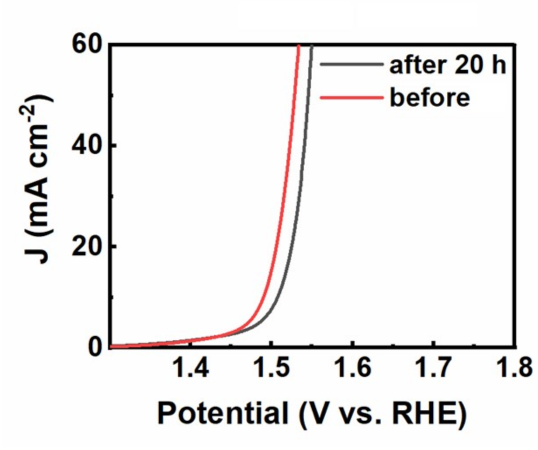

Fig. S12. LSV curves of Ir-W@Ir-WO_{3-x} before (red) and after (black) 20 h CP test.

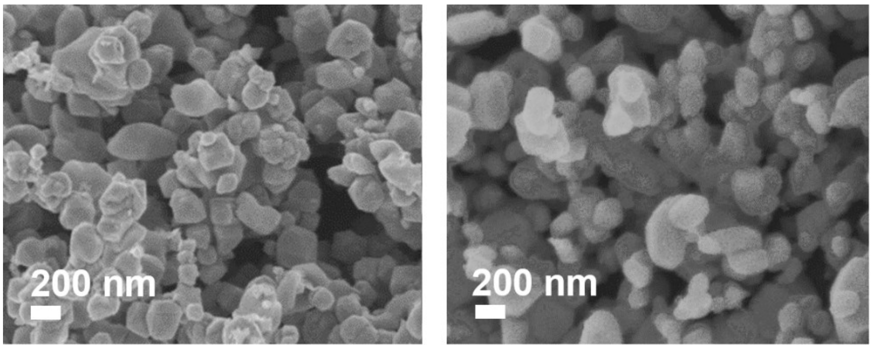

Fig. S13. SEM images of Ir-W@Ir-WO_{3-x} NPs before (left) and after (right) 20 h CP test.

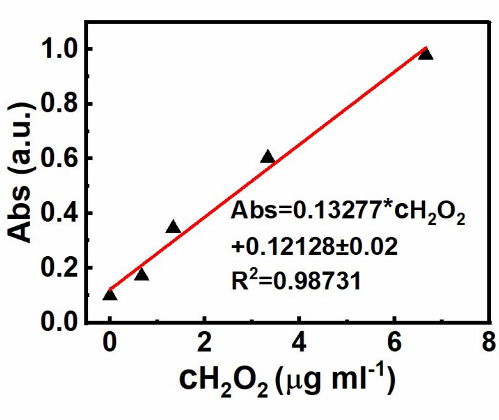

Fig. S14. Standard calibration curve of the UV-vis spectrum absorption intensity versus the concentration of H_2O_2 at 257 nm, to estimate the hydroperoxide.

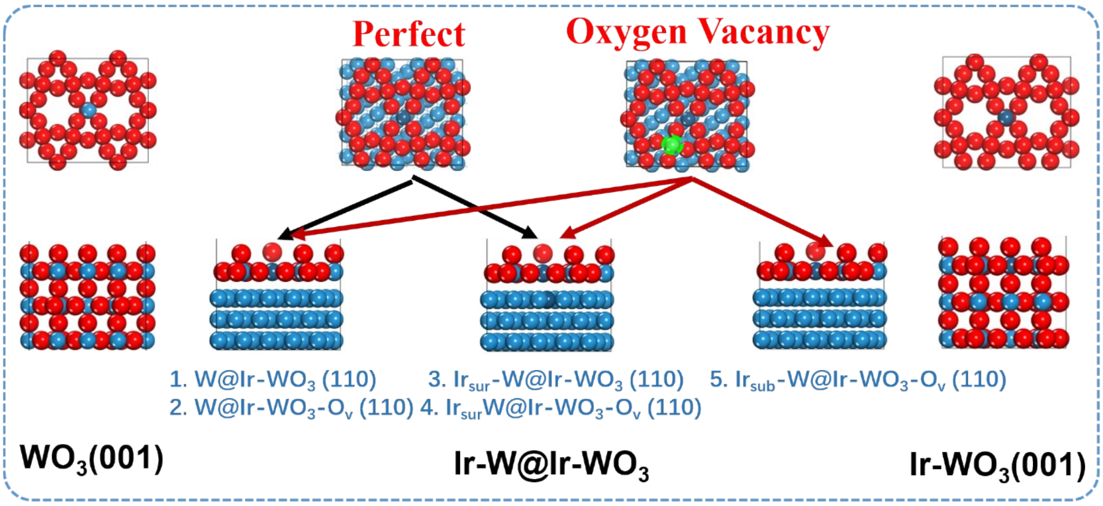

Fig. S15. Structures of WO_3, Ir-WO_3 and Ir-W@Ir-WO_3 surfaces. Dark blue, blue and red balls represent Ir, W and O atoms, respectively. The green dotted lines indicate the location of oxygen vacancies.

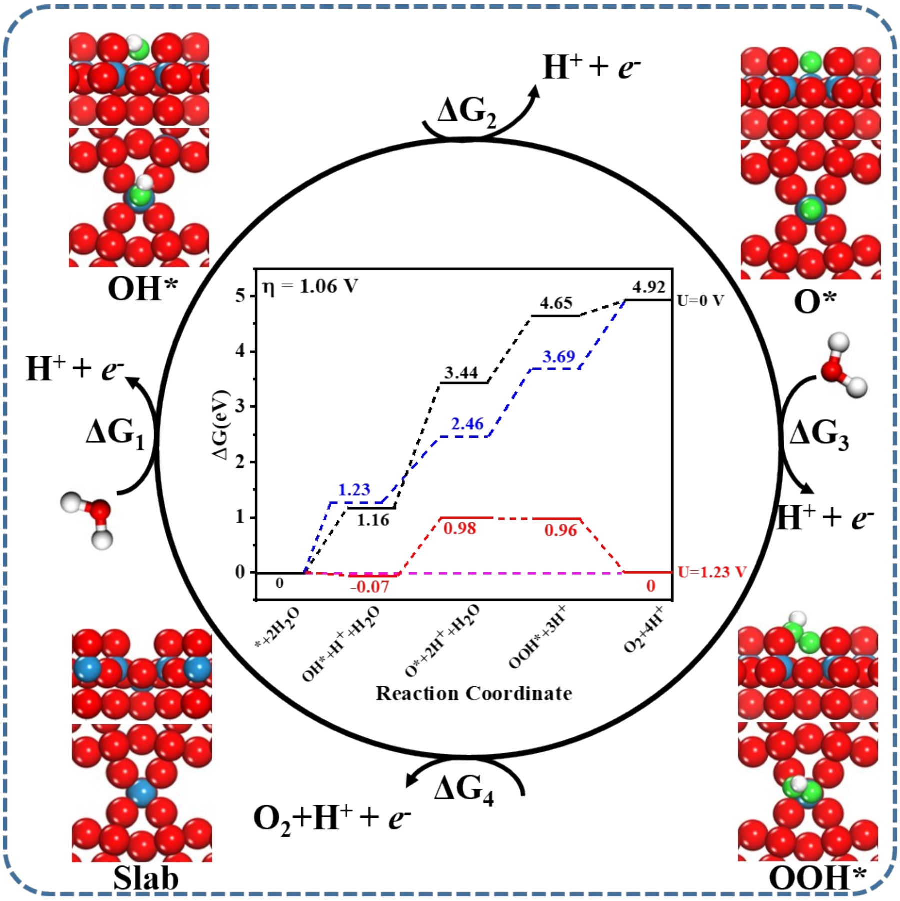

Fig. S16. OER mechanism and the corresponding Gibbs free energy change and adsorption structures on WO_3 (001) surface. The blue and red balls denote W and O atoms, respectively. Green and while balls are O and H atoms involving in the reaction, respectively.

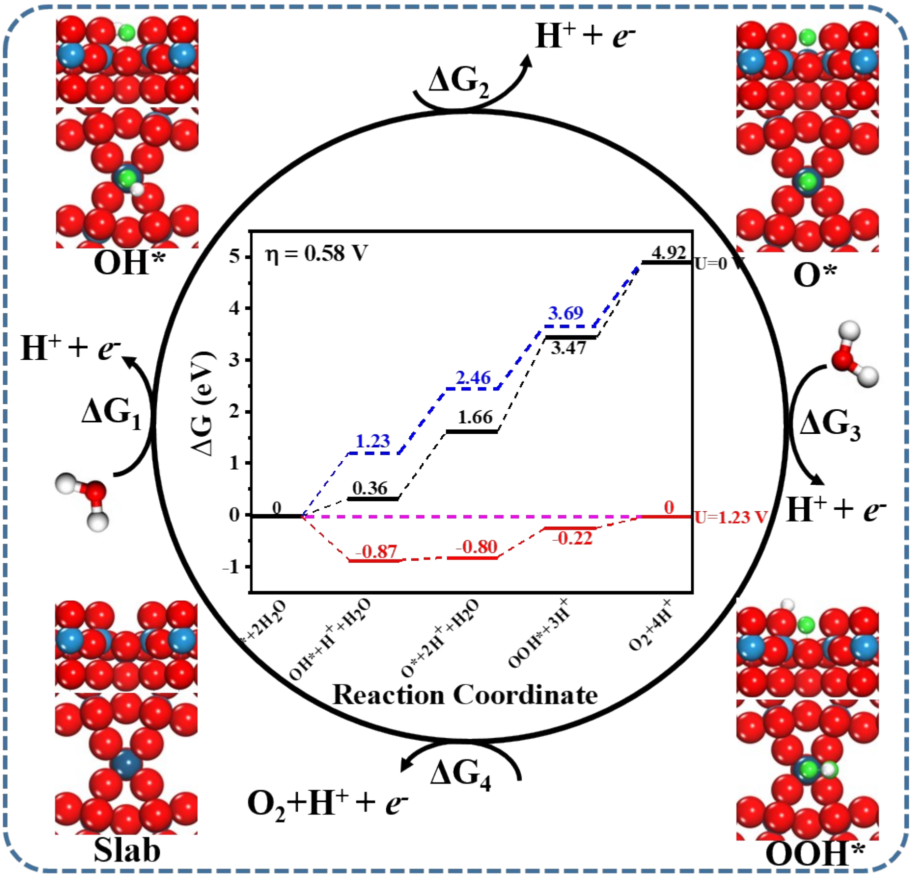

Fig. S17. OER mechanism and the corresponding Gibbs free energy change and adsorption structures on Ir-WO_3 (001) surface. The dark blue, blue and red balls denote Ir, W and O atoms, respectively.

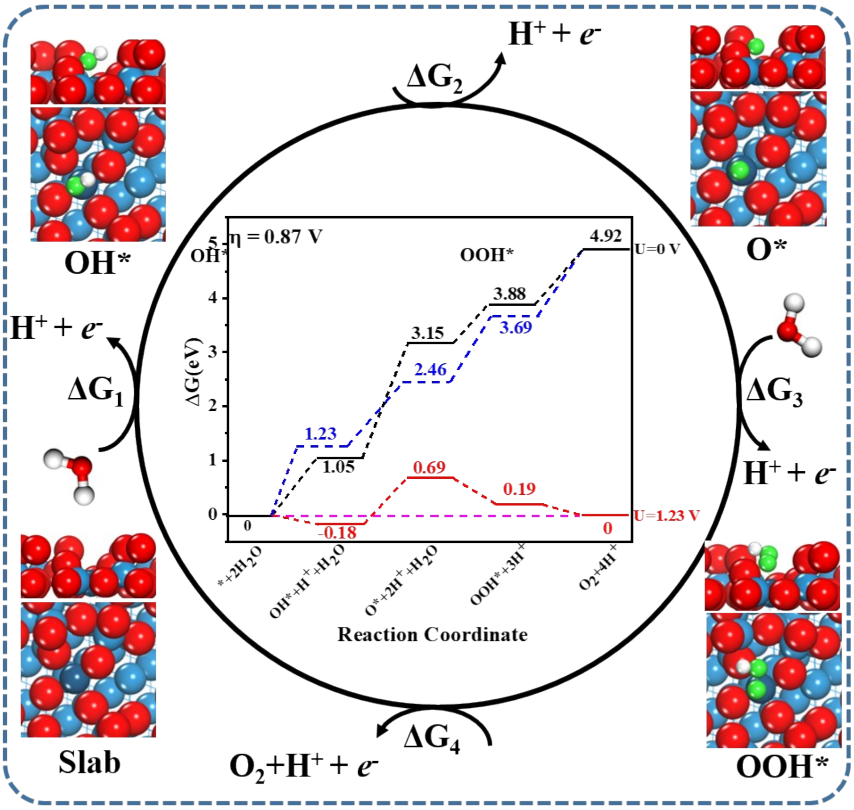

Fig. S18. OER mechanism and the corresponding Gibbs free energy change and adsorption structures on W@Ir-WO_3 (110) surface.

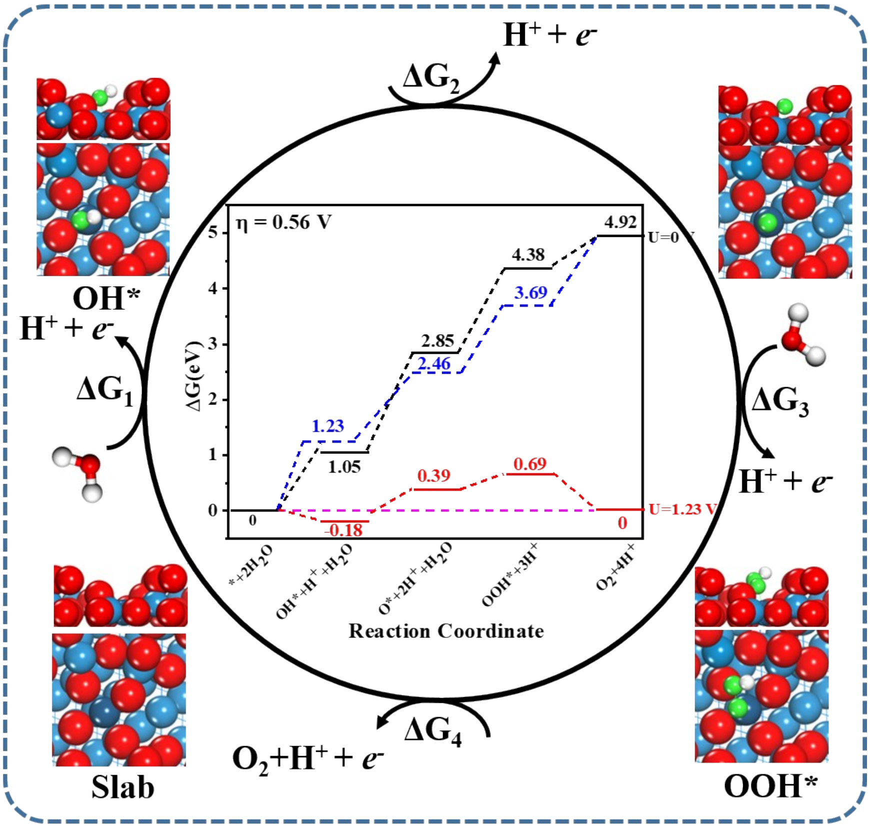

Fig. S19. OER mechanism and the corresponding Gibbs free energy change and adsorption structures on W@Ir-WO_3-O_v (110) surface.

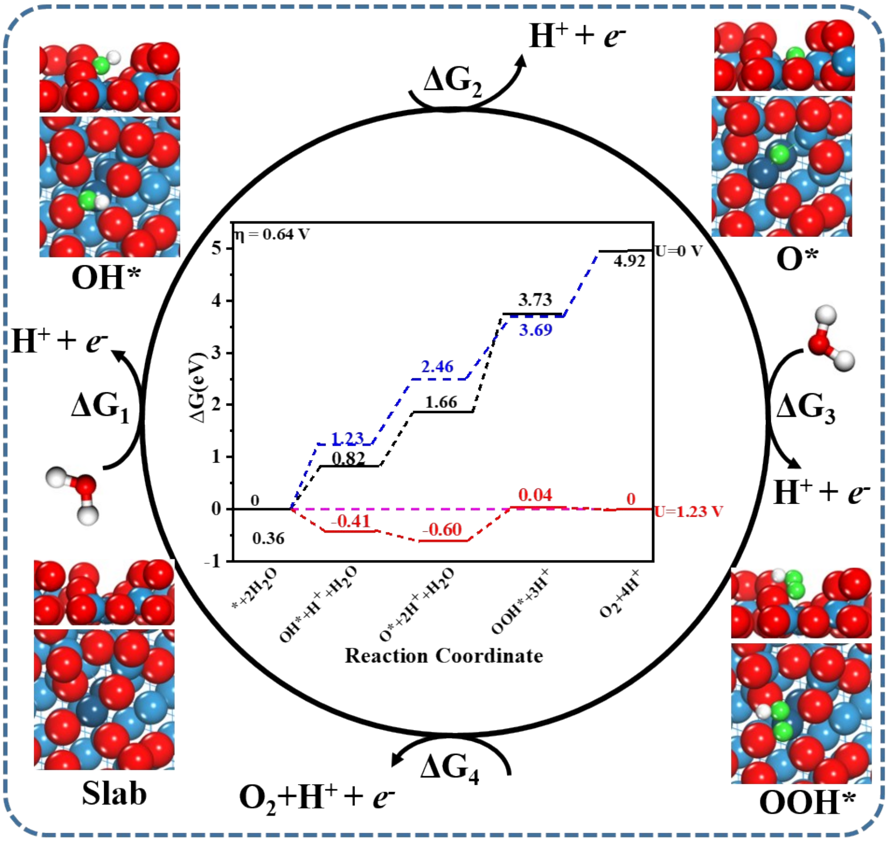

Fig. S20. OER mechanism and the corresponding Gibbs free energy change and adsorption structures on Ir$_{sur}$-W@Ir-WO$_3$ (110) surface.

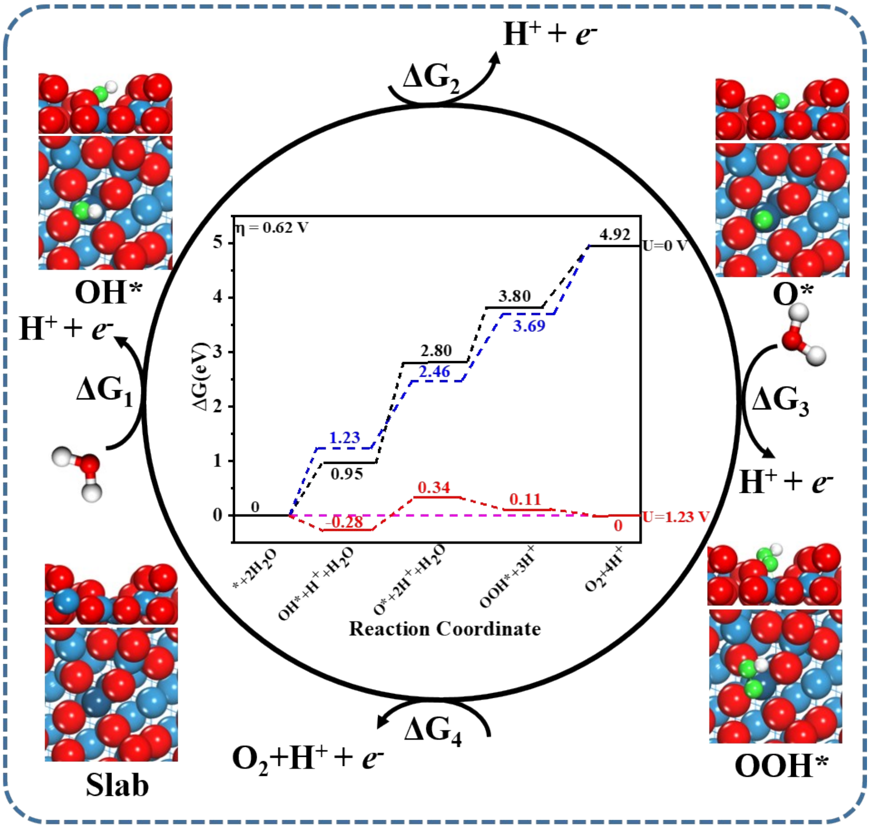

Fig. S21. OER mechanism and the corresponding Gibbs free energy change and adsorption structures on Ir_{sur}-W@Ir-WO_3-O_v (110) surface.

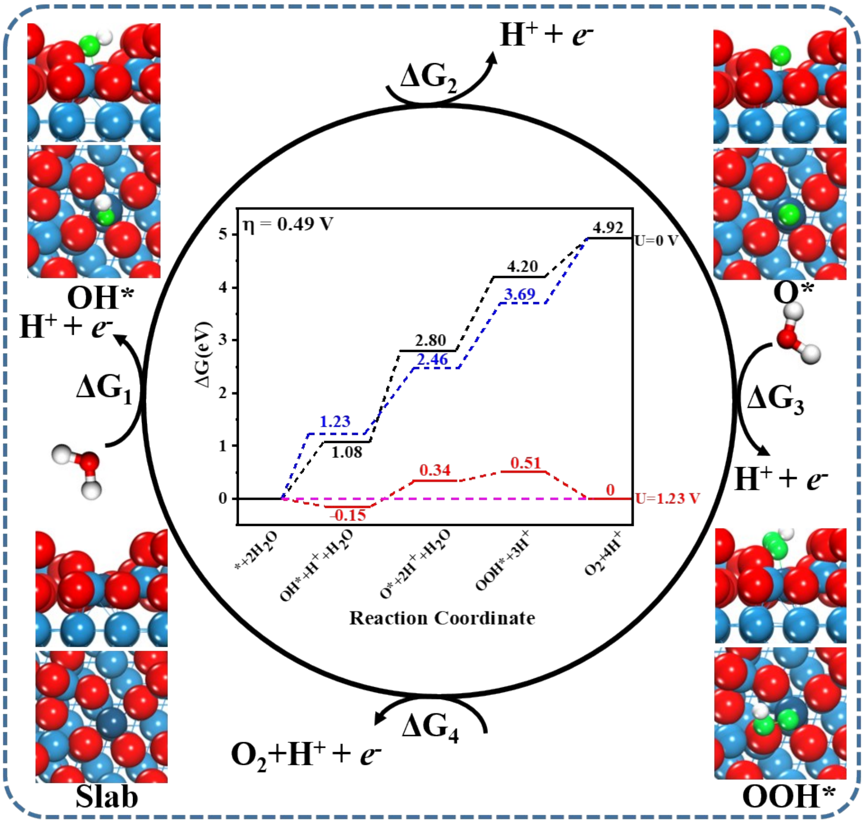

Fig. S22. OER mechanism and the corresponding Gibbs free energy change and adsorption structures on Ir_{sub}-W@Ir-WO_3-O_v (110) surface.

Table S1. The OER performance comparison of Ir-W@Ir-WO_{3-x} with the ever-reported catalysts in acidic condition.

Catalysts	Overpotentials at 10 mA cm^{-2} (mV)	Overpotential upraise after 20 h （mV）	Electrolyte	Ref.
Ir-W@Ir-WO_{3-x}	**261**	**13**	**0.5 M H_2SO_4**	**This work**
SrTi(Ir)O_3	265	50	0.1 M $HClO_4$	11
$SrCo_{0.9}Ir_{0.1}O_{3-\delta}$	270	40	0.1 M $HClO_4$	12
6H-$SrIrO_3$	248	22	0.5 M H_2SO_4	13
IrO_x-$SrIrO_3$	270	20	0.5 M H_2SO_4	14
Ba_2YIrO_6	330	30	0.1 M $HClO_4$	15
$W_{0.57}Ir_{0.43}O_{3-\delta}$	370	20	1.0 M H_2SO_4	16
IrO_2	435	675 (2 h)	0.5 M H_2SO_4	17
RuO_2	370	685 (2 h)	0.5 M H_2SO_4	

References

1 S. Rajagopal, H. M. Lee, K. Lee, C. K. Kim, Hydrothermal synthesis of one-dimensional tungsten oxide nanostructures using cobalt ammonium sulfate as a structure-directing agent, *Korean J. Chem. Eng.*, 2013, **30**, 1833-1835.

2 Y. Wu, J. Cai, Y. Xie, S. Niu, Y. Zang, S. Wu, Y. Liu, Z. Lu, Y. Fang, Y. Guan, X. Zheng, J. Zhu, X. Liu, G. Wang, Y. Qian, Regulating the interfacial electronic coupling of Fe_2N via orbital steering for hydrogen evolution catalysis, *Adv. Mater.*, 2020, **32**, 1904346.

3 G. Telep, D. F. Boltz, Ultraviolet spectrophotometric determination of cobalt with peroxide and bicarbonate, *Anal. Chem.*, 1952, **24**, 945-947.

4 H. Chen, L. Shi, X. Liang, L. Wang, T. Asefa, X. Zou, Optimization of active sites via crystal phase, composition, and morphology for efficient low-iridium oxygen evolution catalysts, *Angew. Chem. Int. Ed. Engl.*, 2020, **59**, 19654-19658.

5 J. Rossmeisl, Z. W. Qu, H. Zhu, G. J. Kroes, J. K. Nørskov, Electrolysis of water on oxide surfaces, *J. Electroanal. Chem.*, 2007, **607**, 83-89.

6 Y. Yao, S. Hu, W. Chen, Z. Q. Huang, W. Wei, T. Yao, R. Liu, K. Zang, X. Wang, G. Wu, W. Yuan, T. Yuan, B. Zhu, W. Liu, Z. Li, D. He, Z. Xue, Y. Wang, X. Zheng, J. Dong, C. R. Chang, Y. Chen, X. Hong, J. Luo, S. Wei, W. X. Li, P. Strasser, Y. Wu, Y. Li, Engineering the electronic structure of single atom Ru sites via compressive strain boosts acidic water oxidation electrocatalysis, *Nat. Catal.*, 2019, **2**, 304-313.

7 R. Kishore, X. Cao, X. Zhang, A. Bieberle-Hütter, Electrochemical water oxidation on WO_3 surfaces: A density functional theory study, *Catal. Today*, 2019, **321-322**, 94-99.

8 Z. W. Seh, J. Kibsgaard, C. F. Dickens, I. Chorkendorff, J. K. Norskov, T. F. Jaramillo, Combining theory and experiment in electrocatalysis: Insights into materials design, *Science*, 2017, **355**, eaad4998.

9 O. Hurtado-Aular, A. B. Vidal, A. Sierraalta, R. Añez, Periodic DFT study of water adsorption on m-WO_3(001), m-WO_3(100), h-WO_3(001) and h-WO_3(100). Role of hydroxyl groups on the stability of polar hexagonal surfaces. *Surf. Sci.* 2020**, 694,** 121558.

10 F. Wang, C. Di Valentin, G. Pacchioni, DFT Study of Hydrogen Adsorption On the Monoclinic WO_3 (001) Surface. *J. Phys. Chem. C* 2012**, 116**, 10672-10679.

11 X. Liang, L. Shi, Y. Liu, H. Chen, R. Si, W. Yan, Q. Zhang, G. D Li, L. Yang, X. Zou, Activating Inert Nonprecious Perovskites with Iridium Dopants for Efficient Oxygen Evolution Reaction under Acidic Conditions. *Angew. Chem. Int. Ed. Engl.* 2019**, 58**, 7631-7635.

12 Y. Chen, H. Li, J. Wang, Y. Du, S. Xi, Y. Sun, M. Sherburne, J. W. Ager, A. C. Fisher, Z. J. Xu, Exceptionally active iridium evolved from a pseudo-cubic perovskite for oxygen evolution in acid. *Nat. Commun.* 2019**, 10**, 572.

13 L. Yang, G. Yu, X. Ai, W. Yan, H. Duan, W. Chen, X. Li, T. Wang, C. Zhang, X. Huang, J. S. Chen, X. Zou, Efficient oxygen evolution electrocatalysis in acid by a perovskite with face-sharing IrO6 octahedral dimers. *Nat. Commun.* 2018**, 9**, 5236.

14 L. C. Seitz, C. F. Dickens, K. Nishio, Y. Hikita, J. Montoya, A. Doyle, C. Kirk, A. Vojvodic, H. Y. Hwang, J. K. Norskov, T. F. Jaramillo, A highly active and stable $IrO_x/SrIrO_3$ catalyst for the oxygen evolution reaction. *Science* 2016, **353**, 1011-1014.

15 O. Diaz-Morales, S. Raaijman, R. Kortlever, P. J. Kooyman, T. Wezendonk, J. Gascon, W. T. Fu, M. T.Koper, Iridium-based double perovskites for efficient water oxidation in acid media. *Nat. Commun.* 2016**, 7**, 12363.

16 S. Kumari, B. P.Ajayi, B. Kumar, J. B. Jasinski, M. K. Sunkara, J. M. Spurgeon, A low-noble-metal $W_{1-x}Ir_xO_{3-\delta}$ water oxidation electrocatalyst for acidic media via rapid plasma synthesis. *Energy Environ. Sci.* 2017, **10**, 2432-2440.

17 J. Shan, C. Guo, Y. Zhu, S. Chen, L. Song, M. Jaroniec, Y. Zheng, S. Z.Qiao, Charge-Redistribution-Enhanced Nanocrystalline Ru@IrO_x Electrocatalysts for Oxygen Evolution in Acidic Media. *Chem* 2019, **5**, 445-459.